Journal of Magnetic Resonance **137,** 358–372 (1999)
Article ID jmre.1998.1679, available online at http://www.idealibrary.com on IDEAL®

# Spin Echo Analysis of Restricted Diffusion under Generalized Gradient Waveforms: Planar, Cylindrical, and Spherical Pores with Wall Relaxivity

S. L. Codd and P. T. Callaghan

*Institute of Fundamental Sciences–Physics, Massey University, Palmerston North, 11222, New Zealand*

Received July 28, 1998; revised December 1, 1998

**A simple matrix formalism presented by Callaghan [*J. Magn. Reson.* 129, 74–84 (1997)], and based on the multiple propagator approach of Caprihan *et al.* [*J. Magn. Reson. A* 118, 94–102 (1996)], allows for the calculation of the echo attenuation, $E(q)$, in spin echo diffusion experiments, for practically all gradient waveforms. We have extended the method to the treatment of restricted diffusion in parallel plate, cylindrical, and spherical geometries, including the effects of fluid–surface interactions. In particular, the $q$-space coherence curves are presented for the finite-width gradient pulse PGSE experiment and the results of the matrix calculations compare precisely with published computer simulations. It is shown that the use of long gradient pulses ($\delta \sim a^2/D$) create the illusion of smaller pores if a narrow pulse approximation is assumed, while ignoring the presence of significant wall relaxation can lead to both an underestimation of the pore dimensions and a misidentification of the pore geometry.** 

## INTRODUCTION

The influence of boundary restrictions on fluid diffusivity has important implications for the modeling of fluid transport in porous media. The NMR signals obtained from the interpenetrating fluid in a porous medium are also strongly influenced by boundary effects. For example, in imaging and microimaging experiments edge enhancement effects may result (*1–3*). In gradient spin echo measurements of restricted diffusion, the pore morphology can impart a characteristic signature which permits the use of these measurements to obtain structural insight via a diffraction formalism (*4–6*). In relaxation measurements the effects of differential relaxivity at the pore surface and within the fluid bulk can provide information about pore surface-to-volume ratios (*7*). The use of such NMR phenomena is well-established in food science, in petroleum engineering, in biomedicine, and in materials science (*8*).

Any effective application of these methods depends on the precision of theory used in the data analysis. In practice the application of gradient spin echo and microimaging experiments to the study of porous media can be severely limited because of some experimental constraints which arise directly from the requirements of the theory. In particular the description of the signal dependence on pore morphology has depended, until very recently, on the need for gradient pulses to be sufficiently narrow in time that the distances diffused by the molecules are insignificant compared to the pore dimensions. Because the distances probed are inversely related to the area under gradient pulses, and because the magnitudes of these pulses tend to be limited by coil and current capabilities, this temporal limitation has restricted both the time and the distance scales accessible to gradient spin echo NMR. A relaxation of the narrow pulse condition would provide access to length scales on the order of or less than 10 $\mu$m. Furthermore, if the theory could be adapted to deal with any gradient waveform modulation whatsoever, then the interpretation of imaging data would be more precise and the use of, for example, oscillatory waveforms, could lead to the use of new frequency domain methods which would provide access to the submillisecond timescale (*9, 10*).

Recently a theoretical method was proposed by Caprihan *et al.* (*11*) which has the potential to address these difficulties. In their approach the gradient waveform is notionally subdivided into a sequence of narrow gradient impulses and evolution periods in which no gradient is present. This trick permits the use of successive propagators for the spin motion sandwiched between evolution operators describing the phase displacements caused by each impulse. The great advantage of such a decomposition is that it allows one to embed all the necessary information about boundary influence to the spin motion in the form of the propagators, each of which may be expressed in eigenmodes of the solutions to the diffusion equation under appropriate boundary conditions. In a subsequent article (*12*) one of us showed that this trick could be expressed in a very simple mathematical language based on the use of matrix multiplication. Indeed, for any gradient waveform whatsoever, only three matrices, $R$, $S$, and $A$, need be calculated and the final expression for the echo attenuation can be written down in a closed form comprising a product of these matrices which is simply related to the known gradient modulation. Furthermore the numerical calculation of this attenuation takes only seconds



1090-7807/99 $30.00

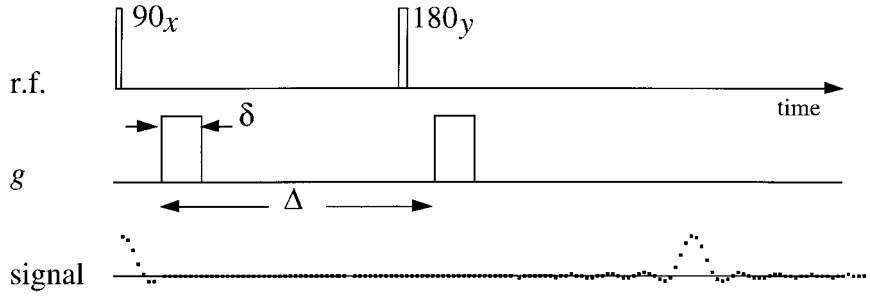


**FIG. 1.** Representation of the standard two-pulse PGSE experiment.

using modern matrix multiplication packages such as "Matlab." In that earlier article these matrices were presented for the case of molecules constrained within planar pores in the absence of wall relaxation and the results so obtained agreed precisely with computer simulations of the pulsed gradient spin echo (PGSE) NMR experiment (*13*) under finite pulse duration conditions. In a later publication (*14*) we have demonstrated similar agreement with the results of microimaging experiments on rectangular pores in which significant edge-enhancement effects were present.

We now present exact analytic forms for $R$, $S$, and $A$ in the case of all three geometries of practical significance, the sphere, cylinder, and plane, and allow in these expressions for the effects of wall relaxivity. The eigenmodes for these problems are well-known (*15*) and we use these to calculate the relevant matrix element expressions, verifying the numerical results of our calculations by comparison with published computer simulations (*16*), in the case of perfectly reflecting walls. Given the known influence of wall relaxation effects on the relevant eigenmode parameters, this particular verification for each of the three geometries helps provide confidence in the entire theory.

## PROPAGATORS FOR RESTRICTED DIFFUSION

The key mathematical tool used to describe the motion of molecules undergoing restricted diffusion is the conditional propagator, $P_s(\mathbf{r}|\mathbf{r}', t)$, an ensemble-averaged probability density for spin displacement from $\mathbf{r}$ to $\mathbf{r}'$ over a time, $t$. $P_s(\mathbf{r}|\mathbf{r}', t)$ obeys the initial condition,

$$P_s(\mathbf{r}|\mathbf{r}', 0) = \delta(\mathbf{r} - \mathbf{r}'), \qquad [1]$$

along with the Ficks' law differential equation,

$$D\nabla'^2 P_s = \partial P_s/\partial t. \qquad [2]$$

This equation may be solved using the standard eigenmode expansion (*17*)

$$P_s(\mathbf{r}|\mathbf{r}', t) = \sum_{n=0}^{\infty} \exp(-\lambda_n t) u_n(\mathbf{r}) u_n^*(\mathbf{r}'), \qquad [3]$$

where the $u_n(\mathbf{r})$ are orthonormal set of solutions to the Helmholtz equation parameterized by the eigenvalue $\lambda_n$ and are subject to the identity

$$\delta(\mathbf{r} - \mathbf{r}') = \sum_{n=0}^{\infty} u_n(\mathbf{r}) u_n^*(\mathbf{r}'). \qquad [4]$$

The eigenvalues $\lambda_n$ depend on the boundary condition for the case of relaxing walls, namely (*7*)

$$D\hat{\mathbf{n}} \cdot \nabla P_s + MP_s = 0, \qquad [5]$$

where $\hat{\mathbf{n}}$ is the outward surface normal and $M$ is the usual wall relaxation parameter (*7*). Using these relationships Eq. [1] has been solved exactly in the case of molecules diffusing within parallel planes, cylinders, and spheres and closed form expressions for these geometries have been derived (*15*, *18–20*).

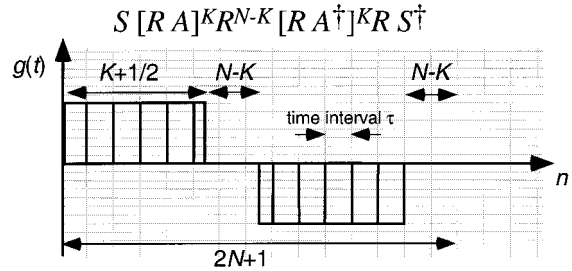


**FIG. 2.** Schematic illustration of impulse decomposition of the finite pulse width PGSE experiment in which $q_{TOT} = (N + 1)q$, $\Delta = (N + \frac{1}{2})\tau$, and $\delta = (K + \frac{1}{2})\tau$. Breaking the waveform into typically 100 impulses allows the echo attenuation to be calculated rapidly while providing suitable digitization of the gradient pulses.

## THE IMPULSE-PROPAGATOR SCHEME

In order to explain the impulse-propagator method it is helpful to begin with the standard two-pulse PGSE experiment, shown in Fig. 1, in which the gradient is applied as two narrow impulses of amplitude **G,** duration $\delta$, and time separation $\Delta$. For this experiment the normalized echo signal is given by (*6, 21*)

$$E(\mathbf{q}) = \int\int d\mathbf{r}d\mathbf{r}'\rho(\mathbf{r})\,P_s(\mathbf{r}|\mathbf{r}',\,\Delta) \times \exp(i2\pi\mathbf{q}\cdot\mathbf{r})\exp(-i2\pi\mathbf{q}\cdot\mathbf{r}'), \quad [6]$$

where $\mathbf{q} = (2\pi)^{-1}\gamma\mathbf{G}\delta$ and $\rho(\mathbf{r})$ is the probability distribution of starting positions.

In the impulse-propagator scheme (*12*), the propagator description of motion is retained in the case of generalized gradient waveforms. For generalized gradient and RF pulse trains, one may speak of an effective gradient $\mathbf{g}(t)$ such that the effect of phase-inverting 180° RF pulses can be mimicked by simply using gradient pulses of opposite sign (while the effect of 90° RF pulses is to switch the gradient off). The impulse-propagator trick involves approximating the gradient waveform, $\mathbf{g}(t)$, by a succession of impulses, such that the time integral of this succession provides a good representation of the $\int \mathbf{g}(t)dt$. By this means the molecular translational motion is subdivided into a sequence of $N$ discrete time intervals $\tau$ bounded by the gradient impulses $\mathbf{q}_n$, $\mathbf{q}_{n+1}$, etc., with all spin phase evolution taking place at well-defined times at the boundaries of those intervals, and with all molecular motion occurring during the intervening periods, in the absence of phase evolution. This approach permits the use of the narrow pulse approximation of Eq. [6] for each migration period. The $\mathbf{q}$ values are determined by digitizing the waveform amplitude $\mathbf{g}(n\tau)$ into units of dimension $\mathbf{g}_{\text{step}}$. At time $n\tau$ the impulse will be $\mathbf{q}_n = m_n\mathbf{q}$ where $\mathbf{q} = (2\pi)^{-1}\gamma\delta\mathbf{g}_{\text{step}}$ and $m_n$ is some positive or negative integer, depending on the local magnitude and sign of $\mathbf{g}(n\tau)$ and given by

$$m_n = \text{integ}(\mathbf{g}(n\tau))/\mathbf{g}_{\text{step}}. \quad [7]$$

By this means the echo amplitude at the end of the sequence may be written

$$E = \int d\mathbf{r}_1 \int d\mathbf{r}_2 \ldots \int d\mathbf{r}_{N+1} \times \rho(\mathbf{r}_1)\exp(i2\pi\mathbf{q}_1\cdot\mathbf{r}_1)\,P_s(\mathbf{r}_1|\mathbf{r}_2,\,\tau) \times \exp(i2\pi\mathbf{q}_2\cdot\mathbf{r}_2)\,P_s(\mathbf{r}_2|\mathbf{r}_3,\,\tau) \ldots \exp(i2\pi\mathbf{q}_N\cdot\mathbf{r}_N)\,P_s(\mathbf{r}_N|\mathbf{r}_{N+1},\,\tau) \times \exp(i2\pi\mathbf{q}_{N+1}\cdot\mathbf{r}_{N+1}). \quad [8]$$

As shown in Ref. (*12*) once the eigenmode representation is used to describe the propagators one obtains the simple matrix product

$$E = S(\mathbf{q})\,R[A(\mathbf{q})]^{m_2}\ldots R[A(\mathbf{q})]^{m_n} \ldots R[A(\mathbf{q})]^{m_N}RS^{\dagger}(-\mathbf{q}), \quad [9]$$

where

$$S_k(\mathbf{q}) = V^{-1/2}\int d\mathbf{r}u_k(\mathbf{r})\exp(i2\pi\mathbf{q}\cdot\mathbf{r}) \quad [10a]$$

$$R_{kk} = \exp(-\lambda_k\tau) \quad [10b]$$

$$A_{kk'}(\mathbf{q}) = \int d\mathbf{r}u_k^*(\mathbf{r})u_{k'}(\mathbf{r})\exp(i2\pi\mathbf{q}\cdot\mathbf{r}) \quad [10c]$$

and $V$ is the pore volume.

The beauty of Eq. [9] is that any waveform may be handled, provided that we calculate just three matrices, $R(\tau)$, $S(\mathbf{q})$, and $A(\mathbf{q})$, where $\mathbf{q}$ is the smallest impulse used to digitize the waveform. The shape of the waveform is then expressed via the indices $m_n$ in accordance with Eq. [7], with negative effective gradients represented by Hermitan conjugation (i.e., $A(-\mathbf{q}_n) = A(\mathbf{q}_n)^{\dagger}$.

The finite gradient pulse waveform is shown in Fig. 2. It is broken into $2N + 1$ intervals so that the total effective scattering wave vector amplitude is $q_{\text{TOT}} = (K + 1)q$, with $\Delta = (N + \frac{1}{2})\tau$ and $\delta = (K + \frac{1}{2})\tau$. Hence

$$E = S(\mathbf{q})[RA(\mathbf{q})]^K R^{N-K}[RA^{\dagger}(\mathbf{q})]^K RS^{\dagger}(\mathbf{q}). \quad [11]$$

## CALCULATION OF MATRIX ELEMENTS FOR SPECIFIC GEOMETRIES

### *Planes*

Originally the matrix formalism was applied to the case of restricted diffusion between parallel plates with perfectly reflecting walls. The extended results presented here allow for relaxation at the fluid–surface interface.

The eigenfunction solutions for parallel plates with nonreflecting walls, that can be found in Ref. (*15*), are

$$u_n(z) = \alpha_n\cos\left(2\xi_n\frac{z}{a}\right) \quad [12a]$$

$$v_m(z) = \beta_m\sin\left(2\zeta_m\frac{z}{a}\right), \quad [12b]$$

where $\alpha_n$ and $\beta_m$ are the normalization coefficients,

$$\alpha_n = \sqrt{\frac{2}{a\left(1 + \frac{\sin 2\xi_n}{2\xi_n}\right)}} \quad \text{and} \quad \beta_m = \sqrt{\frac{2}{a\left(1 + \frac{\sin 2\zeta_m}{2\zeta_m}\right)}} \qquad [13]$$

and $\xi_n$ and $\zeta_m$ are the roots to the transcendental equations

$$\xi_n \tan \xi_n = \frac{Ma}{D} \quad \text{and} \quad \zeta_m \cot \zeta_m = -\frac{Ma}{D}. \qquad [14]$$

Incorporation of relaxation at the walls corresponds to a nonzero value for $M$.

These eigenfunctions are substituted into Eqs. [10a] to [10c] and evaluated for the case of a magnetic field gradient applied normal to the walls, with $q = |\mathbf{q}|$,

$$S_n(q) = V^{-1/2}\alpha_n \int_{a/2}^{a/2} \cos\left(\frac{2\xi_n z}{a}\right) \exp(i2\pi qz)dz$$

$$= \sqrt{\frac{2}{(1 + [\sin(2\xi_n)/2\xi_n])}} \times \left[\frac{(\pi qa \sin(\pi qa)\cos \xi_n) - (\xi_n \cos(\pi qa)\sin \xi_n)}{(\pi qa)^2 - \xi_n^2}\right] \qquad [15a]$$

$$S_m(q) = V^{-1/2}\beta_m \int_{a/2}^{a/2} \sin\left(\frac{2\zeta_m z}{a}\right) \exp(i2\pi qz)dz$$

$$= i\sqrt{\frac{2}{(1 - [\sin(2\zeta_m)/2\zeta_m])}} \times \left[\frac{(\zeta_m \sin(\pi qa)\cos \zeta_m) - (\pi qa \cos(\pi qa)\sin \zeta_m)}{(\pi qa)^2 - \xi_m^2}\right] \qquad [15b]$$

$$R_{nn} = \exp\left(-4\xi_n^2 \frac{D\tau}{a^2}\right) \qquad [15c]$$

$$R_{mm} = \exp\left(-4\zeta_m^2 \frac{D\tau}{a^2}\right) \qquad [15d]$$

$$A_{nn'}(q) = \alpha_n \alpha_{n'} \int_{-a/2}^{a/2} \cos\left(2\xi_n \frac{z}{a}\right) \times \cos\left(2\xi_{n'} \frac{z}{a}\right) \exp(i2\pi qz)dz$$

$$= \frac{1}{2}\sqrt{\frac{2}{(1 + [\sin(2\xi_n)/2\xi_n])}}\sqrt{\frac{2}{(1 + [\sin(2\xi_{n'})/2\xi_{n'}])}} \times \left[\frac{(\pi qa \sin(\pi qa)\cos(\xi_n + \xi_{n'})) - ((\xi_n + \xi_{n'})\cos(\pi qa)\sin(\xi_n + \xi_{n'}))}{(\pi qa)^2 - (\xi_n + \xi_{n'})^2} + \frac{(\pi qa \sin(\pi qa)\cos(\xi_n - \xi_{n'})) - ((\xi_n - \xi_{n'})\cos(\pi qa)\sin(\xi_n - \xi_{n'}))}{(\pi qa)^2 - (\xi_n - \xi_{n'})^2}\right] \qquad [15e]$$

$$A_{mm'}(q) = \beta_m \beta_{m'} \int_{-a/2}^{a/2} \sin\left(2\zeta_m \frac{z}{a}\right) \times \sin\left(2\zeta_{m'} \frac{z}{a}\right) \exp(i2\pi qz)dz$$

$$= \frac{1}{2}\sqrt{\frac{2}{(1 + [\sin(2\zeta_m)/2\zeta_m])}} \times \sqrt{\frac{2}{(1 + [\sin(2\zeta_{m'})/2\zeta_{m'}])}} \times \left[\frac{(\pi qa \sin(\pi qa)\cos(\zeta_m - \zeta_{m'})) - ((\zeta_m - \zeta_{m'})\cos(\pi qa)\sin(\zeta_m - \zeta_{m'}))}{(\pi qa)^2 - (\zeta_m - \zeta_{m'})^2} - \frac{(\pi qa \sin(\pi qa)\cos(\zeta_m + \zeta_{m'})) - ((\zeta_m + \zeta_{m'})\cos(\pi qa)\sin(\zeta_m + \zeta_{m'}))}{(\pi qa)^2 - (\zeta_m + \zeta_{m'})^2}\right] \qquad [15f]$$

$$A_{nm}(q) = \alpha_n \beta_m \int_{-a/2}^{a/2} \cos\left(2\xi_n \frac{z}{a}\right) \sin\left(2\zeta_m \frac{z}{a}\right) \exp(i2\pi qz)dz$$

$$= \frac{i}{2}\sqrt{\frac{2}{(1 + [\sin(2\xi_n)/2\xi_n])}}\sqrt{\frac{2}{(1 - [\sin(2\zeta_m)/2\zeta_m])}} \times \left[\frac{((\xi_n + \zeta_m)\sin(\pi qa)\cos(\xi_n + \zeta_m)) - (\pi qa \cos(\pi qa)\sin(\xi_n + \zeta_m))}{(\pi qa)^2 - (\xi_n + \zeta_m)^2} + \frac{((\xi_n - \zeta_m)\sin(\pi qa)\cos(\xi_n - \zeta_m)) - (\pi qa \cos(\pi qa)\sin(\xi_n - \zeta_m))}{(\pi qa)^2 - (\xi_n - \zeta_m)^2}\right]. \qquad [15g]$$

The exponential terms along the diagonal of $R$ depend on the roots, $\xi_n$ and $\zeta_m$, and the choice of the digitizing time interval, $\tau$. The narrow pulse approximation requires $\tau \ll a^2/D$, so that significant decay of these exponential terms will only occur when $\xi_n$ and $\zeta_m$ are well in excess of unity. Hence, the truncation to finite matrices is only possible if these diagonal

elements have reduced sufficiently at the point of truncation, the dimension at which this cutoff is chosen being determined by the precision criteria for the fit. If the elements of $R$ (and correspondingly $S(q)$ and $A(q)$) are labeled by the index $\nu$ (or $\mu$), then the eigenfunction associated with each element is determined by arranging that the roots $\xi_n$ and $\zeta_m$ increase with increasing $\nu$. This ensures that the most significant elements are included in the final matrix. In ascending order the roots for planar geometry are $\xi_1, \zeta_1, \xi_2, \zeta_2, \xi_3, \zeta_3, \ldots$, etc. Therefore for odd values of the index $\nu$, $n = (\nu + 1)/2$ and for even values of the index $\nu$, $m = \nu/2$.

From this point $\nu$ and $\mu$ will be used to label the rows and columns of the $S(q)$, $A(q)$, and $R$ matrices.

*Cylinders*

To apply the matrix formalism to the case of restricted diffusion in cylindrical pores it is necessary to obtain solutions for the three matrix operators $S(q)$, $A(q)$, and $R$ using the appropriate cylindrical boundary eigenfunctions (*15*),

$$u_\nu(r) = \alpha_{nn'} J_n\left(\xi_{nn'}\frac{r}{a}\right)\cos n\theta, \qquad [16]$$

where $\alpha_{nn'}$ are the normalization coefficients,

$$a_{nn'} = \left[\left(\frac{2}{\pi a^2}\right)\left(\frac{\xi_{nn'}^2}{J_n(\xi_{nn'})}\right)\Big/\left(\left(\frac{Ma}{D}\right)^2 + \xi_{nn'}^2 - n^2\right)\right]^{1/2} \qquad [17a]$$

$$\alpha_{0n'} = \left[\left(\frac{1}{\pi a^2}\right)\left(\frac{\xi_{0n'}^2}{J_0(\xi_{0n'})}\right)\Big/\left(\left(\frac{Ma}{D}\right)^2 + \xi_{0n'}^2\right)\right]^{1/2}, \qquad [17b]$$

and $\xi_{nn'}$ are the roots of the transcendental

$$\xi_{nn'}\frac{J_n'(\xi_{nn'})}{J_n(\xi_{nn'})} = -\frac{Ma}{D}. \qquad [18]$$

Incorporation of relaxation at the walls corresponds to a nonzero value for $M$.

Substituting these eigenfunctions into Eqs. [10a] to [10c] gives, in the case of a magnetic field gradient applied transverse to the cylinder,

$$S_\nu(q) = V^{-1/2}\alpha_{nn'}\int_0^a J_n\left(\xi_{nn'}\frac{r}{a}\right)r\int_0^{2\pi}\cos n\theta \times \exp(iqr\cos\theta)\,d\theta\,dr \qquad [19a]$$

$$R_{\nu\nu} = \exp\left(-\xi_{nn'}^2\frac{D\tau}{a^2}\right) \qquad [19b]$$

$$A_{\nu\mu}(q) = \alpha_{nn'}\alpha_{kk'}\int_0^a J_n\left(\xi_{nn'}\frac{r}{a}\right)J_k\left(\xi_{kk'}\frac{r}{a}\right)r \times\int_0^2 \cos n\theta\cos k\theta\exp(iqr\cos\theta)\,d\theta\,dr, \qquad [19c]$$

where the gradient direction defines the polar axis such that $\mathbf{q}\cdot\mathbf{r} = qr\cos\theta$.

These integrals may be evaluated to yield

$$S_\nu(q) = 2\pi i^n V^{-1/2}\alpha_{nn'}\left(\frac{1}{\xi_{nn'}^2 - (2\pi qa)^2}\right) \times(\xi_{nn'}J_n(2\pi qa)J_{n+1}(\xi_{nn'}) - qaJ_n(\xi_{nn'})J_{n+1}(2\pi qa)) \qquad [20a]$$

$$R_{\nu\nu} = \exp\left(-\xi_{nn'}^2\frac{D\tau}{a^2}\right) \qquad [20b]$$

$$A_{\nu\mu}(q) = \alpha_{nn'}\alpha_{kk'}\left(\frac{\xi_{nn'}}{2}\right)^n\left(\frac{\xi_{kk'}}{2}\right)^k\pi a^2 \times\sum_{p=0}^{\infty}\frac{\left(-\frac{1}{4}\xi_{nn'}^2\right)^p}{p!\Gamma\left(n+p+\frac{3}{2}\right)}\times\sum_{m=0}^{\infty}\frac{\left(-\frac{1}{4}\xi_{kk'}^2\right)^m}{m!\Gamma\left(m+k+\frac{3}{2}\right)} \times\left(\left(\frac{i}{2}qa\right)^{n+k}\sum_{s=0}^{\infty}\frac{\left(-\frac{1}{4}(qa)^2\right)^s}{s!\Gamma\left(s+l+\frac{3}{2}\right)} \times\left(\frac{1}{(2n+2k+2p+2m+2s+2)}\right) + \left(\frac{i}{2}qa\right)^{|n-k|}\sum_{t=0}^{\infty}\frac{\left(-\frac{1}{4}(qa)^2\right)^t}{t!\Gamma\left(t+l+\frac{3}{2}\right)} \times\left(\frac{1}{(n+k+2p+2m+2t+2)}\right)\right). \qquad [20c]$$

As mentioned previously, the eigenfunction associated with each matrix index $\mu$ or $\nu$ is determined by the requirement for the diagonal elements of $R$ to decrease with increasing $\mu$ or $\nu$. For the cylindrical boundary eigenfunctions each root, $\xi_{nn'}$, is labeled by two indices. For each order, $n$, of the Bessel function there are multiple solutions to the transcendental

**TABLE 1**

| $\nu/\mu$ | $n/k$ | $n'/k'$ | $\xi_{nn'}/\xi_{kk'}$ |
|---|---|---|---|
| 1 | 0 | 0 | 0.00 |
| 2 | 1 | 0 | 1.84 |
| 3 | 2 | 0 | 3.05 |
| 4 | 0 | 1 | 3.83 |
| 5 | 3 | 0 | 4.20 |

*Note.* In the case of cylindrical pores, the eigenfunction associated with each matrix index $\mu$ or $\nu$ is determined by arranging that the root $\xi_{nn'}$ increases with increasing $\nu$. The correspondence between $n$, $n'$, and $\nu$ is shown. $k$ and $k'$ are the indices corresponding to the value of $\mu$.

equation (Eq. [18]) and the second index, $n'$, ranks these solutions in ascending order. The correspondence between $n$, $n'$, and $\nu$ is shown in Table 1 for $\nu = 1$ to 5; $k$ and $k'$ are the indices corresponding to the value of $\nu$ This arrangement ensures the most significant diagonal elements of $R$ are included in the truncated matrix.

*Spheres*

The treatment of restricted diffusion in spherical pores is the most mathematically challenging of the basic geometries (*22*). The three matrix operators $S(\mathbf{q})$, $A(\mathbf{q})$, and $R$ are evaluated using the appropriate spherical boundary eigenfunctions (*15*),

$$u_\nu(r) = \alpha_{nn'} j_n\left(\xi_{nn'}\frac{r}{a}\right) P_n(\cos\theta), \qquad [21]$$

where $\alpha_{nn'}$ are the normalization coefficients,

$$\alpha_{nn'} = \left[\left(\frac{2\pi}{2n+1}\right) a^3 (j_n^2(\xi_{nn'}) - j_{n-1}(\xi_{nn'}) j_{n+1}(\xi_{nn'}))\right]^{-1/2}, \qquad [22]$$

**TABLE 2**

| $\nu/\mu$ | $n/k$ | $n'/k'$ | $\xi_{nn'}/\xi_{kk'}$ |
|---|---|---|---|
| 1 | 0 | 0 | 0.00 |
| 2 | 1 | 0 | 2.08 |
| 3 | 2 | 0 | 3.34 |
| 4 | 0 | 1 | 4.49 |
| 5 | 3 | 0 | 4.51 |

*Note.* In the case of spherical pores, the eigenfunction associated with each matrix index $\mu$ or $\nu$ is determined by arranging that the root $\xi_{nn'}$ increases with increasing $\nu$. The correspondence between $n$, $n'$, and $\nu$ is shown. $k$ and $k'$ are the indices corresponding to the value of $\mu$.

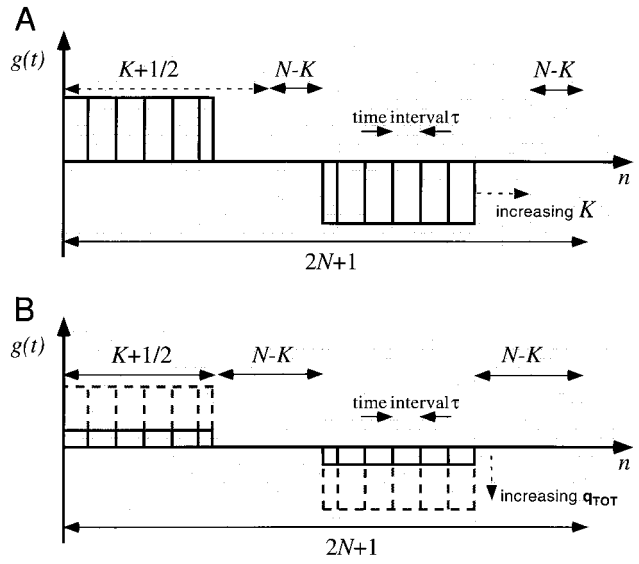


**FIG. 3.** In finite pulse PGSE experiments, **q** space is sampled by successively incrementing the area under the two gradient pulses. This can be achieved by (A) keeping the gradient amplitude, **G,** constant and increasing the pulse duration, $\delta$, or (B) keeping the pulse duration, $\delta$, constant and increasing the gradient amplitude, **G.**

and $\xi_{nn'}$ are the roots of the transcendental

$$\xi_{nn'}\frac{j_n'(\xi_{nn'})}{j_n(\xi_{nn'})} = -\frac{Ma}{D}. \qquad [23]$$

Incorporation of relaxation at the walls corresponds to a nonzero value for $M$.

Substituting these eigenfunctions into Eqs. [10a] to [10c] gives

$$S_\nu(q) = V^{-1/2}\alpha_{nn'}\int_a^a j_n\left(\xi_{nn'}\frac{r}{a}\right) r^2 \times \int_{-1}^{1} P_n(\cos\theta)\exp(iqr\cos\theta)\, d(\cos\theta)\, dr \qquad [24a]$$

$$R_{\nu\nu} = \exp\left(-\xi_{nn'}^2\frac{D\tau}{a^2}\right) \qquad [24b]$$

$$A_{\nu\mu}(q) = \alpha_{nn'}\alpha_{kk'}\int_a^a j_n\left(\xi_{nn'}\frac{r}{a}\right) j_k\left(\xi_{kk'}\frac{r}{a}\right) r^2 \times \int_{-1}^{1} P_n(\cos\theta)\, P_k(\cos\theta) \times \exp(iqr\cos\theta)\, d(\cos\theta)\, dr, \qquad [24c]$$

where again, the gradient direction defines the polar axis.

Using the identities shown in the Appendix, one may evaluate these integrals to obtain

$$S_\nu(q) = 2(i)^{-n}V^{-1/2}\alpha_{nn'}(qa)^{-1/2}\left(\frac{a^3}{\xi_{nn'}^2 - (qa)^2}\right) \times (\xi_{nn'}j_n(qa)j_{n+1}(\xi_{nn'}) - qaj_n(\xi_{nn'})j_{n+1}(qa)) \quad [25a]$$

$$R_{\nu\nu} = \exp\left(-\xi_{nn'}^2\frac{D\tau}{a^2}\right) \quad [25b]$$

$$A_{\nu\mu}(q) = \alpha_{nn'}\alpha_{kk'}\xi_{nn'}^n\xi_{kk'}^k(qa)^{1/2}a^3\left(\frac{1}{2}\right)^{(s/2+n+k)}\Gamma\left(\frac{1}{2}\right) \times \sum_l (i)^{3l}\left(\frac{qa}{2}\right)^{(l+1/2)} \times \frac{(2l+1)\Gamma(c+1)\Gamma\left(c-k+\frac{1}{2}\right) \times \Gamma\left(c-n+\frac{1}{2}\right)\Gamma\left(c-l+\frac{1}{2}\right)}{\Gamma\left(c+\frac{3}{2}\right)\Gamma(c-l+1) \times \Gamma(c-n+1)\Gamma(c-k+1)} \times \sum_{p=0}^{\infty}\frac{\left(-\frac{1}{4}\xi_{nn'}^2\right)^p}{p!\Gamma\left(n+p+\frac{3}{2}\right)} \times \sum_{m=0}^{\infty}\frac{\left(-\frac{1}{4}\xi_{kk'}^2\right)^m}{m!\Gamma\left(m+k+\frac{3}{2}\right)} \times \sum_{s=0}^{\infty}\frac{\left(-\frac{1}{4}(qa)^2\right)^s}{s!\Gamma\left(s+l+\frac{3}{2}\right)} \times \left(\frac{1}{(n+k+l+2p+2m+2s+3)}\right), \quad [25c]$$

where

$$c = \frac{n+k+l}{2},\ |n-k| \le l \le n+k \quad \text{and}$$

$n + k + l$ is odd.

As with the other geometries, the limitation to finite matrices is only possible if the diagonal elements of $R$ have reduced sufficiently at the point of truncation. Accordingly the roots $\xi_{nn'}$ are ordered with increasing magnitude. The root associated with each matrix index $\mu$ or $\nu$ is determined by a particular choice of $n$ and $n'$ (or $k$ and $k'$). Table 2 shows these roots along with the corresponding $n$ and $n'$ for $\nu = 1$ to 5.

## NUMERICAL IMPLEMENTATION

The original publication (*12*) clearly describes the method for determining the matrix product for a given gradient waveform. The expression begins and ends with the $S(q)$ vectors, inside which the appropriate sandwich of $A(q)$ and $R$ matrices is placed. The $S(q)$ and $A(q)$ matrices are calculated for the required geometry by using roots which include the appropriate wall relaxation and a $q$ value corresponding to the waveform digitization. The waveform is broken into $N$ segments of time $\tau$. Typically 100 segments ensures that the resulting discrete waveform function is a valid approximation to the continuous waveform. It is also important that $\tau$ be less than the "characteristic timescales." These are, respectively, the times $a^2/D$, $a/M$, and $[(\gamma g)^2D]^{-1/3}$ (*23*).

In order that the narrow pulse approximation is valid for each interval it is of course necessary that $\tau \ll a^2/D$. However in most PGSE experiments designed to probe diffraction effects, it is sufficient that $\Delta \sim a^2/D$ and unnecessary that $\Delta \gg a^2/D$. Hence, dividing the interval $\Delta$ by 100 easily satisfies the first condition. $\tau \ll a/M$ is equivalent to requiring $Ma/D \ll N$. Given $N = 100$ in our calculation, this condition is certainly satisfied since for $Ma/D \sim N$ the relaxation attenuation would be so severe that the experiment would be impractical. Establishing the third condition is more subtle. To observe diffraction it is necessary that $q_{max}a \sim \pi$ and $\Delta \sim a^2/D$. It is unnecessary that $q_{max}a \gg \pi$ or $\Delta \gg a^2/D$ and so we will neglect these possibilities. The two conditions $q_{max}a \sim \pi$ and $\Delta \sim a^2/D$ lead directly to the requirement $[(\delta^2\Delta)/(2\pi^2)^2]^{1/3} \ll [(\gamma g)^2D]^{-1/3}$ and as $\delta \le \Delta$ this gives $0.14\delta \ll [(\gamma g)^2D]^{-1/3}$. Provided $\delta$ is subdivided into at least 10 intervals of $\tau$, then $\tau \le [(\gamma g)^2D]^{-1/3}$ and $\tau \ll [(\gamma g)^2D]^{-1/3}$ is easily satisfied for most finite pulse cases where $\delta/\tau \sim 100$.

In the matrix calculations effective closure is achieved down the diagonal of the $R$ matrix by approximately the 20th element. If it is necessary to decrease the time interval further then larger matrices are required and the computational time increases accordingly. The $S(q)$ and $A(q)$ matrices were calculated in a *c*-programme, requiring several minutes of computing time on a PowerMac, and the matrix product was evaluated in the matrix-handling package, Matlab. Matlab handles long matrix products with ease, evaluating $E(q)$ at 50 values of $q$, for trains of one hundred $20 \times 20$ matrices, in only a few seconds. Any of the code can be provided by contacting P.Callaghan@massey.ac.nz.

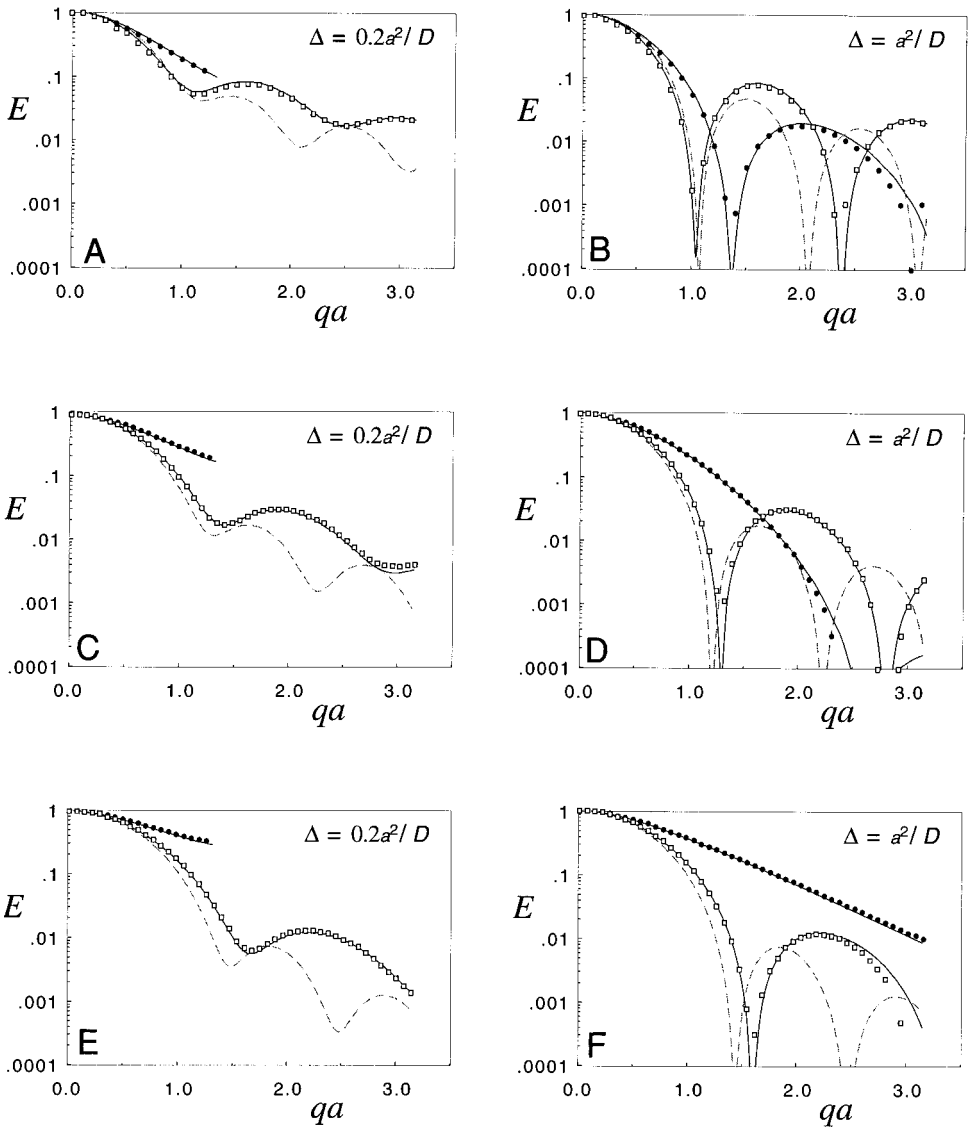


**FIG. 4.** The results of the matrix calculations are displayed as solid lines and compared absolutely with discrete points taken from the Monte Carlo simulations of Linse and Söderman (*16*). The $q$ values are changed by altering the duration of the gradient pulse as demonstrated in Fig. 3A. The echo attenuation $E(q)$ is shown for $\Delta = 0.2\ a^2/D$ and $\Delta = a^2/D$ for (A) and (B) planar, (C) and (D) cylindrical, and (E) and (F) spherical geometries. The solid circles correspond to $\gamma^* g^* = 40$ and the open squares correspond to $\gamma^* g^* = 200$. The broken lines have been added for reference to indicate the narrow pulse limit.

## COMPARISON WITH SIMULATIONS

The results of the matrix calculations were verified by comparing them with Monte Carlo computer simulations published by Linse and Söderman (*16*). These simulations present $E(\mathbf{q})$, with $\mathbf{q}$ values successively increased by keeping the gradient amplitude, $\mathbf{G}$, constant and varying the duration, $\delta$, of the gradient pulse; see Fig. 3A. The matrix operator expression required to represent their experiment is

$$E(q_{\mathrm{TOT}}, \Delta) = S(q)[R(\tau)A(q)]^K R(\tau)^{N-K} \times [R(\tau)A(q)]^K R(\tau) S(q), \qquad [26]$$

where $q_{\mathrm{TOT}}$ is increased from 0 to $\pi/a$ by setting $q$ to $\pi/K_{\max}a$ and incrementing the integer $K$ from 0 to $K_{\max}$. The ratio $K_{\max}/N = \delta_{\max}/\Delta$. The results for $\Delta = 0.2a^2/D$ and $\Delta = a^2/D$ are shown in Fig. 4 for planar, cylindrical, and spherical pores. Data from the matrix products are displayed as solid lines and discrete points taken from the computer simulations are overlaid. Linse and Söderman define a "dimensionless gradient amplitude," $\gamma^* g^* = \gamma g a^3/D$, which provides an indication of the ratio of $\delta$ to $\Delta$ when $qa = \pi$. For example if $\Delta = a^2/D$ and $\gamma^* g^* = 20$, then $\delta = \Delta$ when $qa = \pi$; see Table 3. The narrow pulse limit of $\gamma^* g^* \to \infty$ is evaluated using the above matrix product with $K = 0$ and $q = q_{\mathrm{TOT}}$ and shown as a

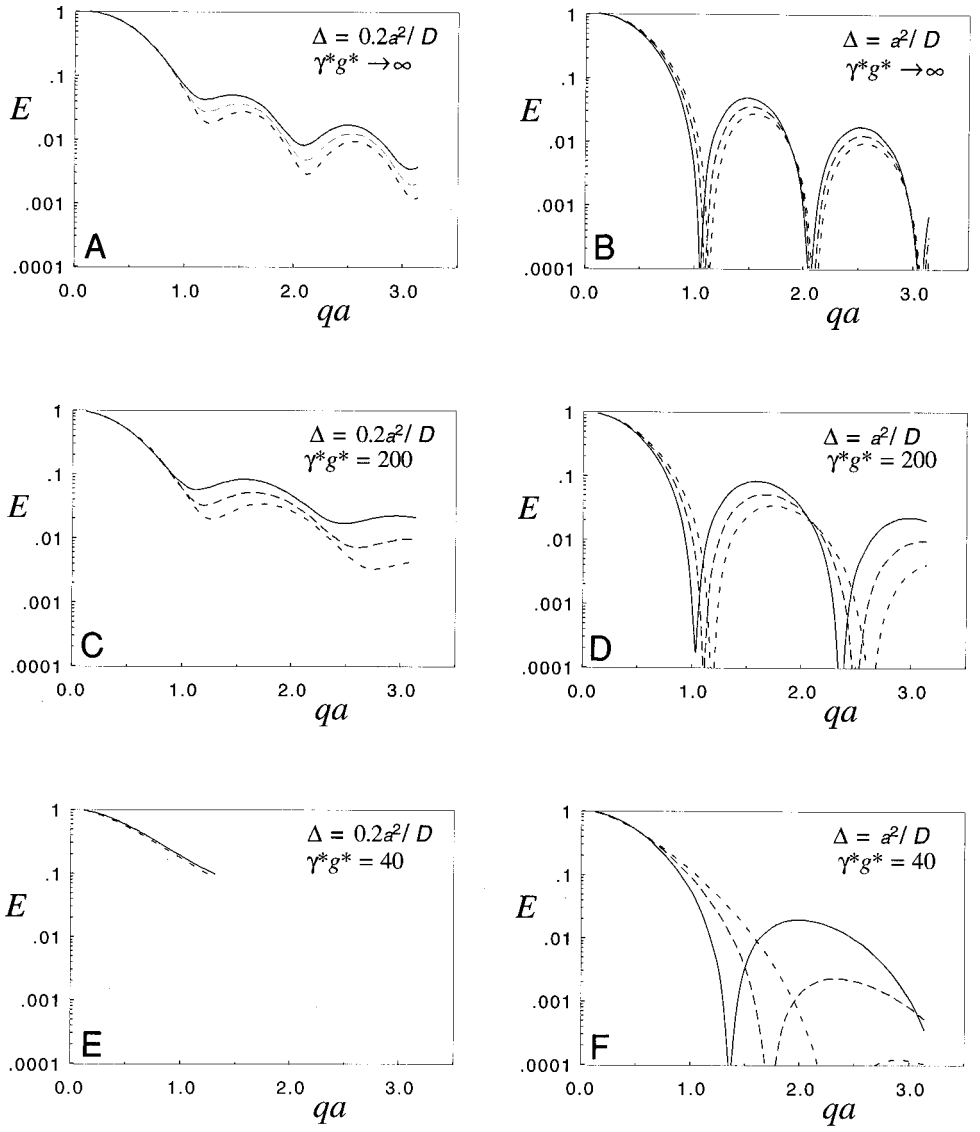


**FIG. 5.** Planar geometry in which the broken lines demonstrate the effect of including relaxation at the pore surfaces for each of the curves in Figs. 4A and 4B. The solid curves are obtained by calculating the roots in Eq. [14] with $Ma/D = 0$, while the dashed curves are for $Ma/D = 1$ and $Ma/D = 2$.

dotted line on each graph. The solid circles in Fig. 4 correspond to $\gamma^*g^* = 40$ and the open squares correspond to $\gamma^*g^* = 200$.

**TABLE 3**

| $\gamma^*g^*$ | $\Delta$ | $\delta/\Delta$ (when $qa = \pi$) |
|---|---|---|
| 40 | 0.2 | 2.5 |
| 40 | 1.0 | 0.5 |
| 200 | 0.2 | 0.5 |
| 200 | 1.0 | 0.1 |

*Note.* $\gamma^*g^*$ gives an indication of the ratio of $\delta$ to $\Delta$ when $qa = \pi$. Because it is not physical for $\delta$ to be greater than $\Delta$, when $\gamma^*g^* = 40$ and $\Delta = 0.2$, then $E(q)$ can only be calculated out to a maximum $q$ value of $0.4\ \pi/a$.

Note that these comparisons involve no fitted parameters. The calculations are absolute. The excellent agreement between the Monte Carlo simulations and the theoretical results in all three geometries provides solid support for the use of the matrix formalism to analyze the finite pulse PGSE experiment.

## EFFECT OF WALL RELAXATION

Many physical systems can be justifiably modeled without allowing for relaxation at the walls. Typical values found in the literature for the NMR surface relaxivity parameter, $M$, are of the order of 1–10 $\mu$ms$^{-1}$ for synthetic materials such as procelain, glass beads, alumina, and silica gels (*24*). For water, where $D \sim 2 \times 10^{-9}$ m$^2$ s$^{-1}$, diffusing in pores of the order

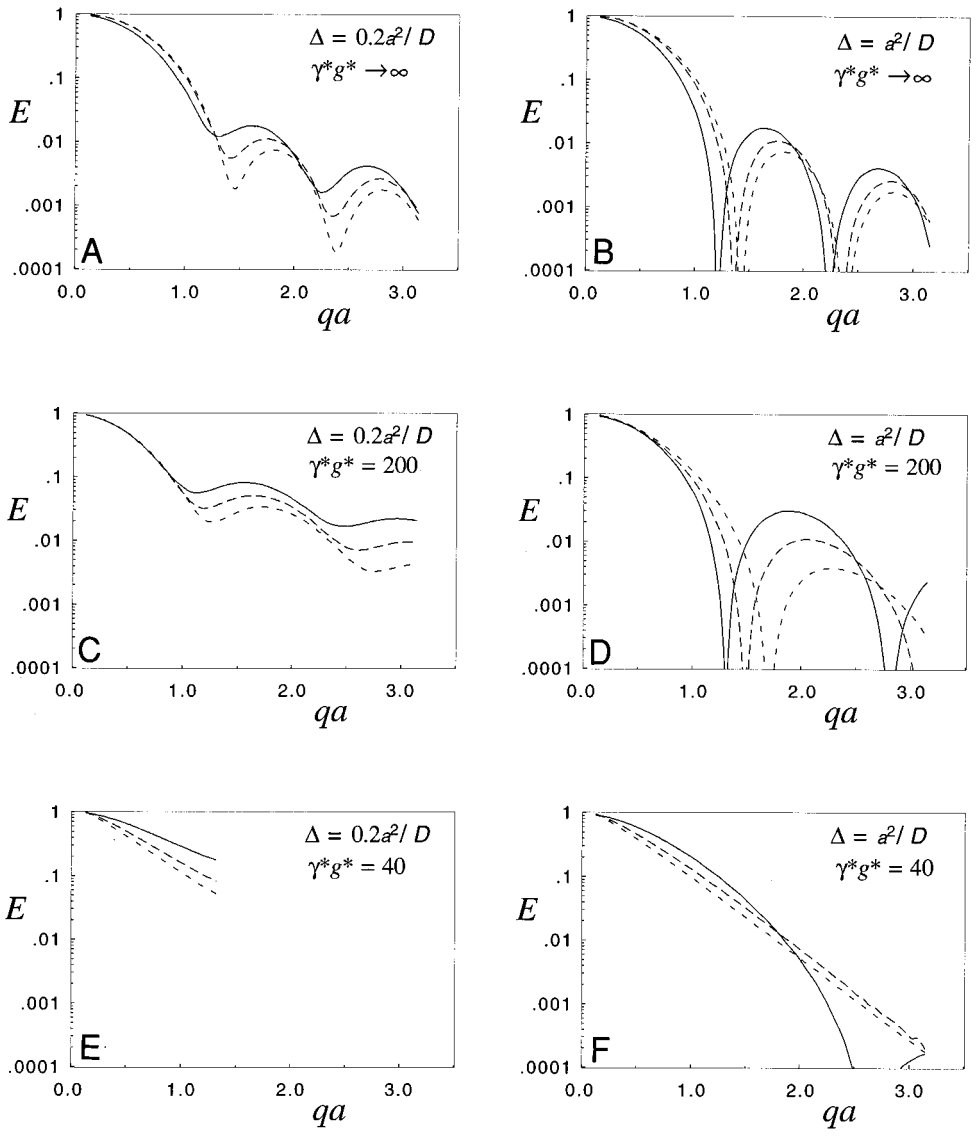


**FIG. 6.** Cylindrical geometry in which the broken lines demonstrate the effect of including relaxation at the pore surfaces for each of the curves in Figs. 4C and 4D. The solid curves are obtained by calculating the roots in Eq. [18] with $Ma/D = 0$, while the dashed curves are for $Ma/D = 1$ and $Ma/D = 2$.

of 10 $\mu$m, then $Ma/D \ll 1$ and a model with reflecting walls is a valid approximation.

The PGSE experiment requires $D\Delta/a^2 \sim 1$ (or $D/a \sim a/\Delta$), if restricted diffusion is to be observed. Therefore we can rewrite the requirement for the perfectly reflecting wall approximation, $Ma/D \ll 1$, as $M\Delta/a \ll 1$. Hence, in systems with smaller pores or slower diffusing fluids, or in materials, such as rocks (*24*) and cement pastes (*25*), where the mineralogy can significantly increase the surface relaxation, the effect cannot necessarily be ignored. Hence, it is useful to have an understanding of the effect and significance of the fluid–surface interaction on the **q**-space data.

## CONSTANT *G* METHOD

It is possible to sample **q** space by holding the gradient amplitude, **G,** constant and varying the duration, $\delta$. This is the experiment described above and which is shown schematically in Fig. 3A. The curves in Fig. 4 show the case where no relaxation occurs at the pore surface. The effect of relaxation, i.e., $Ma/D = 1$ and $Ma/D = 2$ in the eigenvalue equation, can be seen in Figs. 5, 6, and 7 for planar, cylindrical, and spherical pores, respectively. In each graph the solid curves are obtained by calculating the roots in Eqs. [14], [18], and [23] with $Ma/D = 0$, while the dashed curves are for $Ma/D = 1$ and $Ma/D = 2$. As expected, the effect

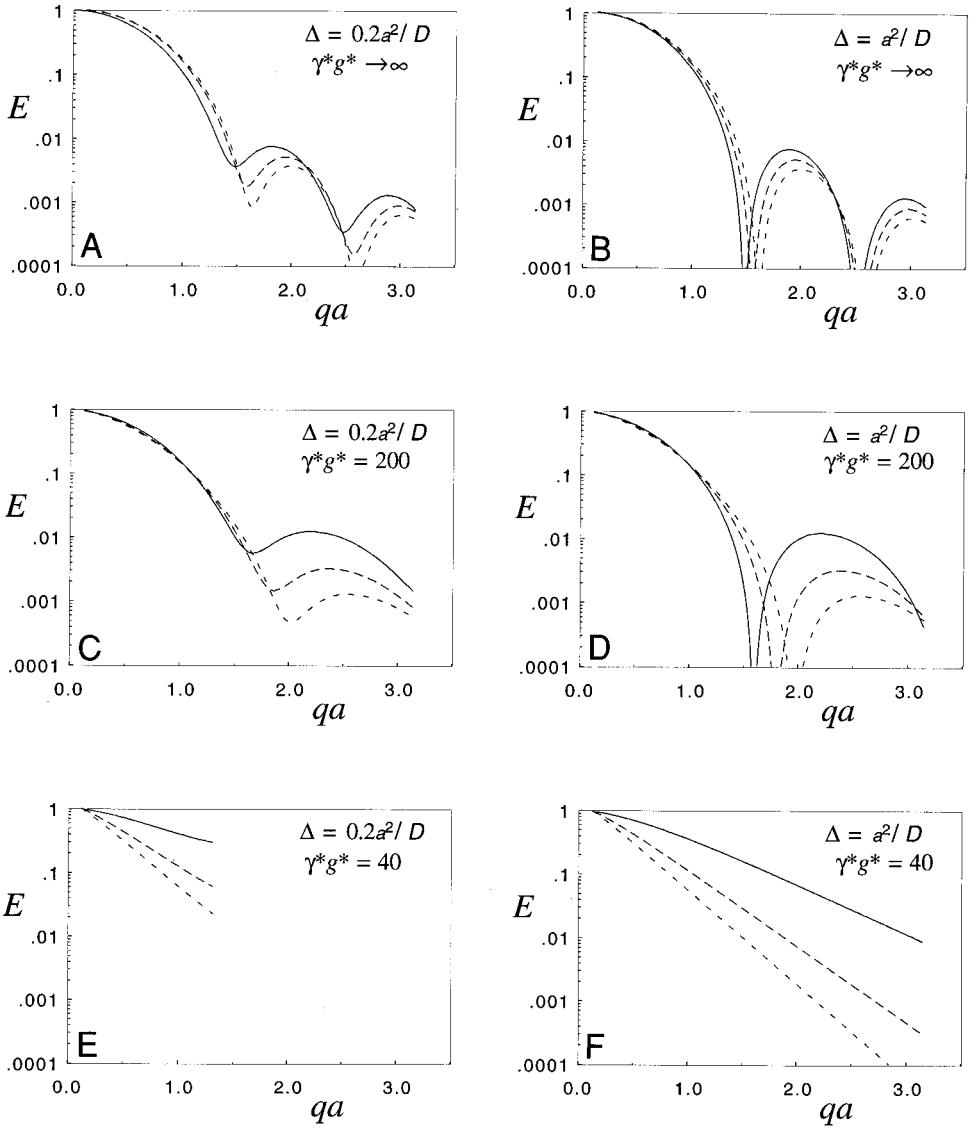


**FIG. 7.** Spherical geometry in which the broken lines demonstrate the effect of including relaxation at the pore surfaces for each of the curves in Figs. 4E and 4F. The solid curves are obtained by calculating the roots in Eq. [23] with $Ma/D = 0$, while the dashed curves are for $Ma/D = 1$ and $Ma/D = 2$.

of significant wall relaxation is an apparent narrowing of the pore and a decrease in the magnitude of the coherence peak.

## CONSTANT $\delta$ METHOD

Alternatively **q** space can be traversed by maintaining a constant gradient pulse duration, $\delta$, and incrementing the amplitude, **G;** see Fig. 3B. Using the matrix formalism this method is represented by the product

$$E(q_{\mathrm{TOT}}, \Delta) = S(q)[R(\tau)A(q)]^K R(\tau)^{N-K} \times [R(\tau)A(q)]^K R(\tau)S(q), \qquad [27]$$

where $q_{\mathrm{TOT}}$ is increased from 0 to $\pi/a$ by stepping $q$ such that $q = q_{\mathrm{TOT}}/K$, the integer $K$ being set such that the ratio $K/N = \delta/\Delta$. The results for $\Delta = 0.2a^2/D$ and $\Delta = a^2/D$ and no wall relaxation are shown in Fig. 8 for planar, cylindrical, and spherical pores. The solid lines are the narrow pulse limits, calculated by setting $K = 0$, and $q = q_{\mathrm{TOT}}$. The dotted lines show the two useful cases of $\delta = \Delta$ and $\delta = 0.5\Delta$.

Figures 9, 10, and 11 show the effect of relaxation at the fluid–surface interface for planar, cylindrical, and spherical geometries, respectively. The solid curves are obtained by calculating the roots from the transcendental equations (Eqs. [14], [18], and [23]) with $Ma/D = 0$, while the dashed curves are for $Ma/D = 1$ and $Ma/D = 2$.

When sampling $q$ space by holding the pulse duration constant, the effective narrowing of the pore is more significant

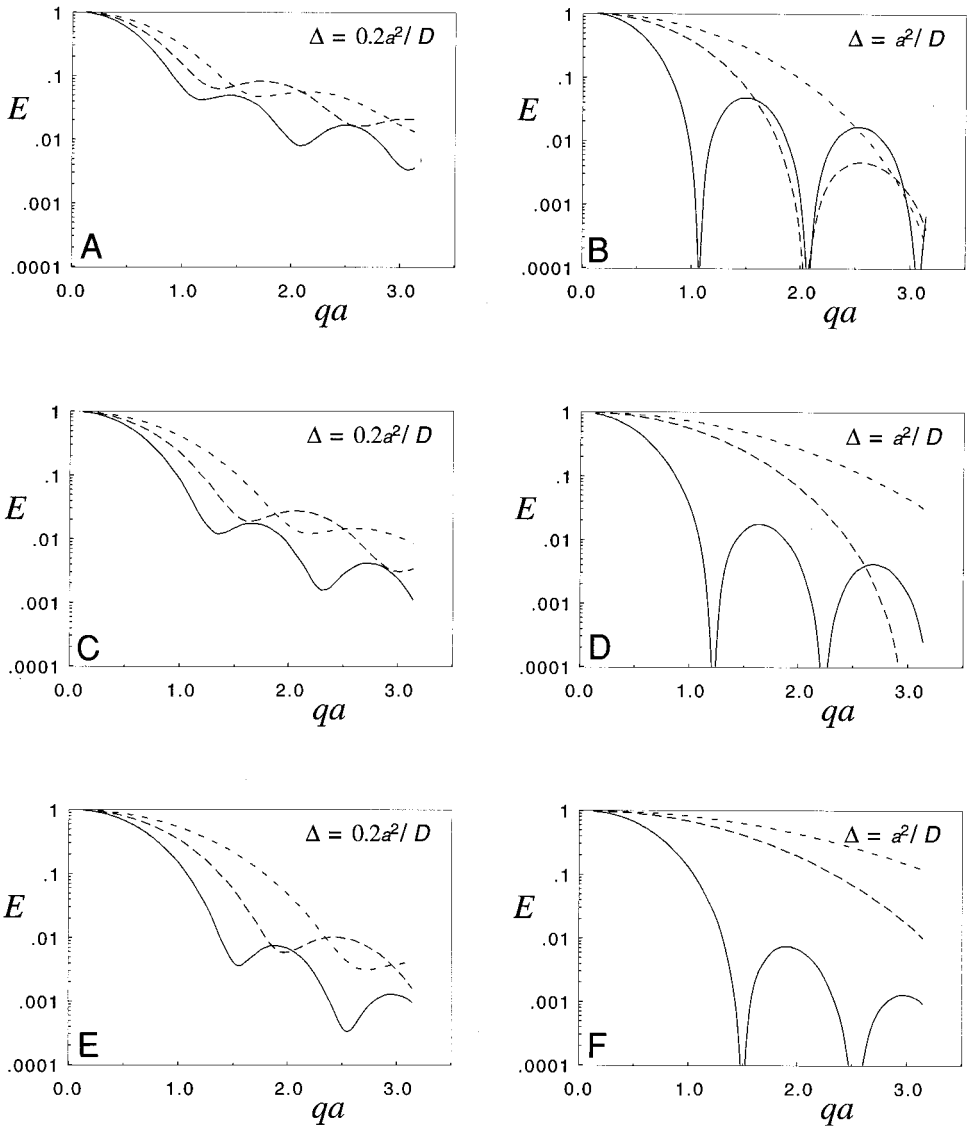


**FIG. 8.** The matrix product is used to predict the results from the finite pulse PGSE experiment shown schematically in Fig. 3B. The $q$ values are increased by increasing the amplitude of the gradient pulses and holding the pulse width constant. The echo attenuation $E(q)$ is shown for $\Delta = 0.2\ a^2/D$ and $D = a^2/D$ for (A) and (B) planar, (C) and (D) cylindrical, and (E) and (F) spherical geometries. The dashed curves correspond to $\delta/\Delta = 0.5$ and $\delta/\Delta = 1.0$. The solid lines have been added for reference to indicate the narrow pulse limit.

than if the gradient amplitude is unaltered, as can be seen by comparing Figs. 4 and 8. The effect of significant wall relaxation is a further narrowing of the apparent pore size and a lowering in magnitude of the first coherence peak. Indeed the magnitude of the peak shows a shift similar to that associated with the pore shape being deformed from planar to cylindrical to spherical, a result which emphasizes the importance of allowing for relaxation effects if the geometrical interpretation is to remain sound.

## CONCLUSIONS

The extension of the impulse-propagator methodology to the case of spherical and cylindrical pores is significant, as is the inclusion of relaxation at the walls. Many natural porous media can be modeled using one of these cases. Spherical and cylindrical geometries are also of particular significance in the study of emulsions and colloidal structures.

The next level in the development of the matrix formalism is to address the problem of interconnected pores. For regular structures, eigenmode expansions are possible in a basis of Bragg waves (*26*). However, for glassy materials where no orientational order exists this route is not possible. Previously the extension of the narrow pulse PGSE experiment to such materials was achieved by means of a pore hopping theory (*5*). The combining of this theory with the impulse-propagator method and hence the extension of the

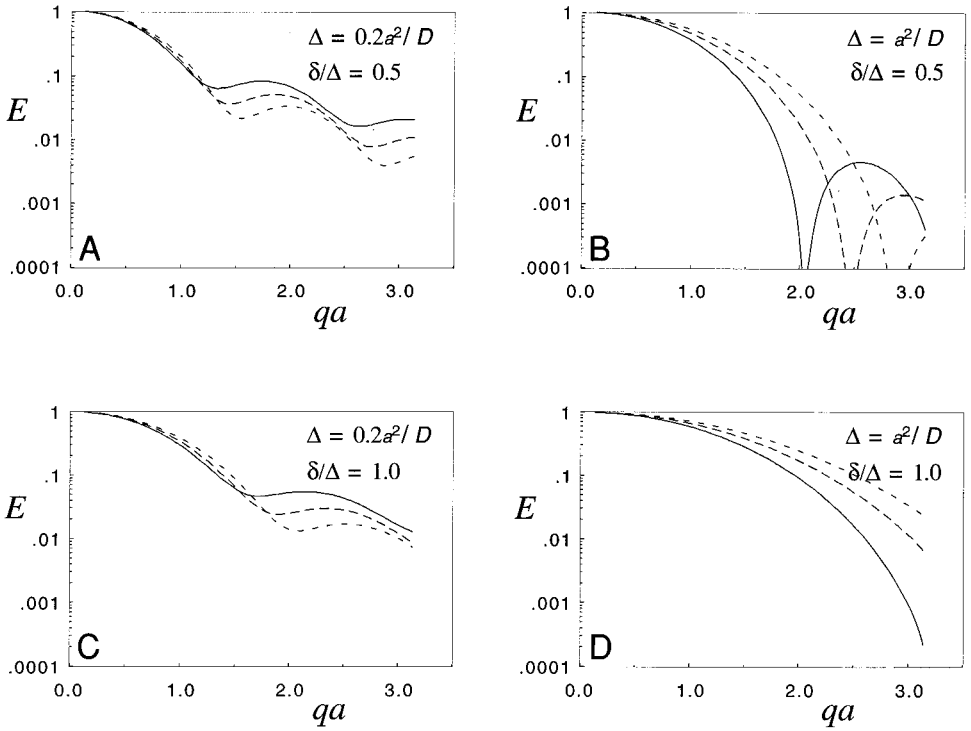


**FIG. 9.** Planar geometry in which the broken lines demonstrate the effect of including relaxation at the pore surfaces for each of the dashed curves in Figs. 8A and 8B. The solid curves are obtained by calculating the roots in Eq. [14] with $Ma/D = 0$, while the dashed curves are for $Ma/D = 1$ and $Ma/D = 2$.

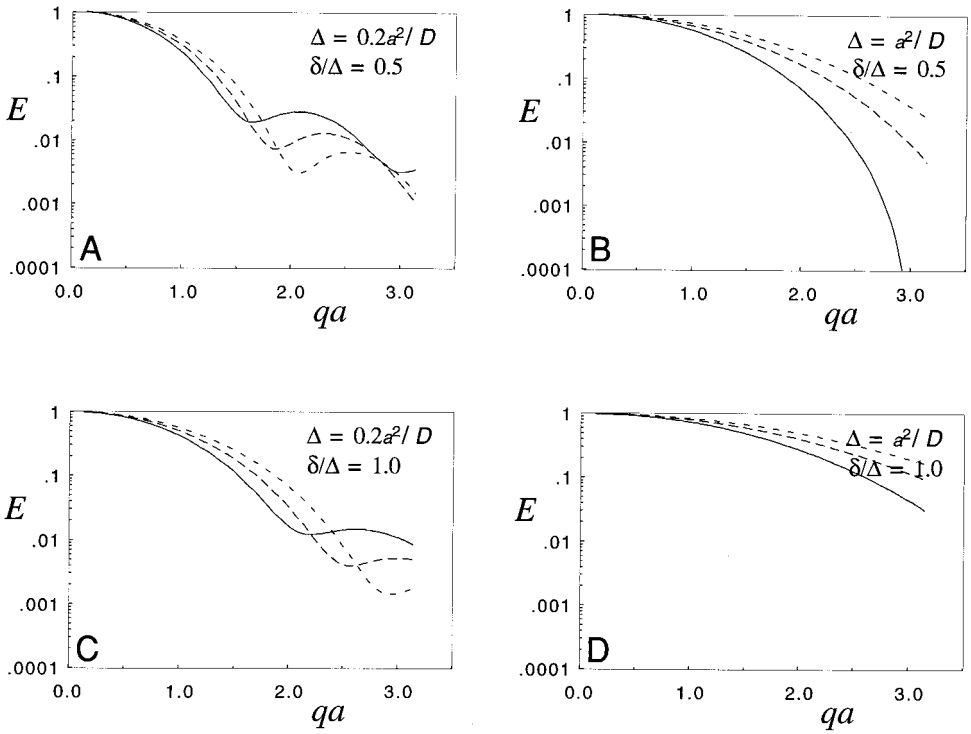


**FIG. 10.** Cylindrical geometry in which the broken lines demonstrate the effect of including relaxation at the pore surfaces for each of the curves in Figs. 8C and 8D. The solid curves are obtained by calculating the roots in Eq. [18] with $Ma/D = 0$, while the dashed curves are for $Ma/D = 1$ and $Ma/D = 2$.

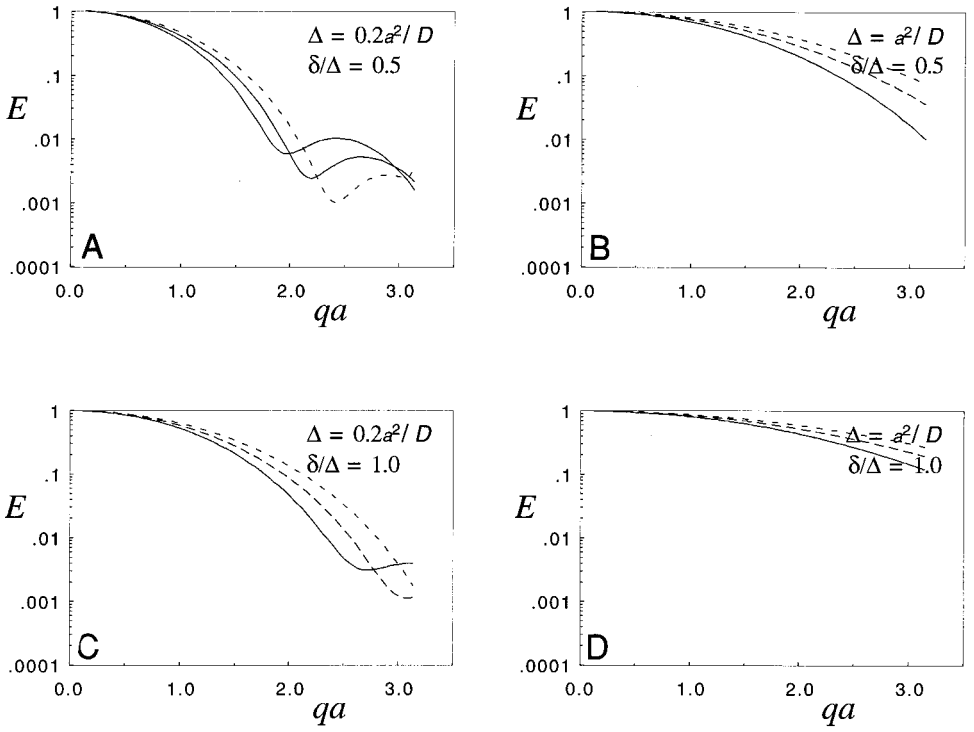


**FIG. 11.** Spherical geometry in which the broken lines demonstrate the effect of including relaxation at the pore surfaces for each of the curves in Figs. 8E and 8F. The solid curves are obtained by calculating the roots in Eq. [23] with $Ma/D = 0$, while the dashed curves are for $Ma/D = 1$ and $Ma/D = 2$.

matrix formalism to porous media will form the basis of a later publication (*27*).

Finally we note that although this method has been presented in the context of PGSE NMR, the matrix approach is ideally suited to handle the theoretical treatment of microimaging experiments. Where gradients of changing orientation are used (as in polar or spatial **q**-space rasters), the formulae could easily be modified to include the effects of gradient impulses in each of the encoding directions. Using the methods outlined in this paper, the analysis of image artifacts, such as edge enhancement due to restricted diffusion, should be straightforward and accurate (*14*).

## APPENDIX

The following identities were used to evaluate $S(q)$ and $A(q)$ for the case of spherical boundary conditions:

$$j_n'(r) = \frac{n}{2n+1} j_{n-1}(r) - \frac{n+1}{2n+1} j_{n+1}(r)$$

$$j_n(r) = \frac{r}{2n+1} (j_{n-1}(r) - j_{n+1}(r))$$

$$j_n(ar) = \sqrt{\frac{\pi}{2ar}} \left(\frac{1}{2} ar\right)^{n+1/2} \sum_{p=0}^{\infty} \left(\frac{(-1/4(ar)^2)^p}{p!\Gamma(n+p+3/2)}\right)$$

$$\int_0^1 j_n(ar) j_n(br) r^2 dr$$

$$= \frac{1}{a^2 - b_2} \left( b\left( j_n(a) j_n'(b) + \frac{1}{2} j_n(a) j_n(b) \right) - a\left( j_n(b) j_n'(a) + \frac{1}{2} j_n(a) j_n(b) \right) \right)$$

$$P_n(\cos\theta) P_k(\cos\theta) = \sum_l a_l P_l(\cos\theta)$$

where

$$a_l = 0 \quad \text{if} \quad |n-k| < l < |n+k| \quad \text{or} \quad (n+k+l)$$

$$= \frac{(2s+1)\Gamma(1/2)\Gamma(s+1)\Gamma(s-n+1/2) \times \Gamma(s-k+1/2)\Gamma(s-l+1/2)}{2\pi^{3/2}\Gamma(s+3/2)\Gamma(s-n+1) \times \Gamma(s-k+1)\Gamma(s-l+1)}$$

for all other $l$

and $s = (n+k+l)/2$.

## ACKNOWLEDGMENTS

The authors are grateful to the New Zealand Foundation for Research, Science, and Technology for financial support. S.L.C. acknowledges the support of a Royal Society of New Zealand, Science and Technology Postdoctoral Fellowship.

## REFERENCES

1. W. B. Hyslop and P. C. Lauterbur, *J. Magn. Reson.* **94,** 501 (1991).
2. B. Pütz, D. Barsky, and K. Schulten, *J. Magn. Reson.* **97,** 27 (1992).
3. P. T. Callaghan, A. Coy, L. C. Forde, and C. J. Rofe, *J. Magn. Reson.* **A110,** 347 (1993).
4. P. T. Callaghan, A. Coy, D. MacGowan, K. J. Packer, and F. O. Zelaya, *Nature* **351,** 467 (1991).
5. P. T. Callaghan, A. Coy, J. P. Halpin, D. MacGowan, K. J. Packer, and F. O. Zelaya, *J. Chem. Phys.* **97,** 651 (1992).
6. P. T. Callaghan, "Principles of Nuclear Magnetic Resonance Microscopy," Oxford Univ. Press, Oxford/New York (1991).
7. K. R. Brownstein and C. E. Tarr, *Phys. Rev. A* **19,** 2446 (1979).
8. B. Blümich, P. Blümler, R. Botto, and E. Fukushima, "Spatially Resolved Magnetic Resonance," VCH, Weinheim (1998).
9. P. T. Callaghan and J. Stepisnik, *J. Magn. Reson.* **117,** 118 (1995).
10. P. T. Callaghan and J. Stepisnik, *Adv. Magn. Opt. Reson.* **19,** 325 (1996).
11. A. Caprihan, L. Z. Wang, and E. Fukushima, *J. Magn. Reson. A* **118,** 94 (1996).
12. P. T. Callahan, *J. Magn. Reson.* **129,** 74 (1997).
13. E. O. Stejskal and J. E. Tanner, *J. Chem. Phys.* **42,** 288 (1965).
14. P. T. Callaghan and S. L. Codd, *J. Magn. Reson. Imaging* **16,** 471 (1998).
15. P. T. Callaghan, *J. Magn. Reson. A* **113,** 53 (1995).
16. P. Linse and O. Söderman, *J. Magn. Reson. A* **116,** 77 (1995).
17. Arfken, "Mathematical Methods for Physicists," Academic Press, New York (1970).
18. J. E. M. Snaar and H. V. As, *J. Magn. Reson. A* **102,** 318 (1993).
19. P. P. Mitra, P. N. Sen, and L. M. Schwartz, *Phys. Rev. B* **47,** 8565 (1993).
20. P. P. Mitra and P. N. Sen, *Phys. Rev. B* **45,** 143 (1992).
21. E. O. Stejskal, *J. Chem. Phys.* **43,** 3597 (1965).
22. S. L. Codd and P. T. Callaghan, *in* "Spatially Resolved Magnetic Resonance: Methods and Applications in Materials Science, Agriculture and Biomedicine" (B. Blümich, P. Blümler, R. Botto, and E. Fukushima, Eds.), VCH, Weinheim (1998).
23. M. D. Hürlimann, K. G. Helmer, T. M. de Swiet, P. N. Sen, and C. H. Sotak, *J. Magn. Reson. A* **113,** 260 (1995).
24. R. L. Kleinberg, *Magn. Reson. Imaging* **14,** 761 (1996).
25. K. S. Mendelson, W. P. Halperin, J. Y. Jehng, and Y. Q. Song, *Magn. Reson. Imaging* **12,** 207 (1994).
26. D. J. Bergman and K. J. Dunn, *Phys. Rev. E* **51,** 3401 (1995).
27. P. T. Callaghan and S. L. Codd, to be submitted (1999).